JCI insight

RESOURCE AND TECHNICAL ADVANCE

Extracellular matrix alterations in chronic ischemic cardiomyopathy revealed by quantitative proteomics

Kevin M. Buck,[1] Holden T. Rogers,[1,2] Zachery R. Gregorich,[2,3] Morgan W. Mann,[4] Timothy J. Aballo,[2,5] Zhan Gao,[2] Emily A. Chapman,[1] Andrew J. Perciaccante,[1,2] Scott J. Price,[2] Ienglam Lei,[6] Paul C. Tang,[6,7] and Ying Ge[1,2,8]

[1]Department of Chemistry, [2]Department of Cell and Regenerative Biology, [3]Department of Animal and Dairy Sciences, [4]Department of Medicine, and [5]Molecular and Cellular Pharmacology Training Program, University of Wisconsin–Madison, Madison, Wisconsin, USA. [6]Department of Physiology and Biomedical Engineering and [7]Department of Cardiac Surgery, Mayo Clinic, Rochester, Minnesota, USA. [8]Human Proteomics Program, School of Medicine and Public Health, University of Wisconsin–Madison, Madison, Wisconsin, USA.

Ischemic cardiomyopathy (ICM) is a leading cause of heart failure characterized by extensive remodeling of the cardiac extracellular matrix (ECM). While initially adaptive, ECM deposition following ischemic injury eventually turns maladaptive, promoting adverse cardiac remodeling. The strong link between the extent of fibrosis and adverse clinical outcomes has led to growing interest in ECM-targeted therapies to prevent or reverse maladaptive cardiac remodeling in ICM; yet, the precise composition of the ECM in ICM remains poorly defined. In this study, we employed sequential protein extraction enabled by the photocleavable surfactant Azo to enrich ECM proteins from left ventricular tissues of patients with end-stage ICM and nonfailing donor hearts. High-resolution mass spectrometry–based quantitative proteomics identified and quantified over 6,000 unique protein groups, including 315 ECM proteins. We discovered significant upregulation of key ECM components, particularly glycoproteins, proteoglycans, collagens, and ECM regulators. Notably, *LOXL1*, *FBLN1*, and *VCAN* were among the most differentially expressed. Functional enrichment analyses revealed enhanced TGFB signaling, integrin-mediated adhesion, and complement activation in ICM tissues, suggesting a feedback loop driving continued ECM deposition in the end-stage failing heart. Together, our findings provide a comprehensive proteomic landscape of ECM alterations in the end-stage ICM myocardium and identify promising molecular targets for therapeutic intervention.

Conflict of interest: YG is a coinventor on patents covering the photocleavable surfactant Azo (US 12,304,884 B2) and its application to extracellular vesicle proteomics (US 12,078,646 B2). KMB is also a coinventor on US 12,078,646 B2. YG has received research funding from AbbVie, Inc., and holds an additional patent (US 20240076553A1). PCT serves as a noncompensated member of the Data Safety Monitoring Board for the XVIVO Perfusion PRESERVE trial and is a coinventor on a US provisional patent titled Histone-acetylation-modulating agents for the treatment and prevention of organ injury (No. 63/045,784; International application PCT/US2021/039650).

Submitted: June 20, 2025
Accepted: September 23, 2025
Published: September 30, 2025

Reference information: *JCI Insight*. 2025;10(21):e196933. https://doi.org/10.1172/jci.insight.196933.

Introduction

Ischemic heart disease (IHD) is the most prevalent form of cardiovascular diseases and remains the leading cause of morbidity and mortality globally (1–3). Its incidence continues to rise mainly due to aging population and prevalence of comorbidities, such as diabetes and obesity, putting an ever-increasing burden on health care systems (1, 3). Ischemic cardiomyopathy (ICM) resulting from chronic coronary artery disease (CAD) and/or acute myocardial infarction (MI) is the most severe clinical manifestation of IHD and the single largest cause of heart failure (HF) (2–4). With current treatments focused primarily on the management of associated symptoms, there is an urgent need to better understand the molecular changes associated with ischemic HF to enable the development of targeted therapies.

Traditionally, the diagnosis of ICM has been based on a history of MI or objective evidence of CAD (5). In ICM, cardiomyocyte death resulting from myocardial ischemia leads to remodeling and increased deposition of extracellular matrix (ECM) (6, 7), a process called fibrosis and primarily driven by myofibroblasts — cardiac fibroblasts activated by growth factors, such as TGFB, or increased mechanical stress (8). While myocardial fibrosis initially reinforces the ventricular wall — preventing rupture — persistent ECM accumulation ultimately becomes maladaptive, promoting adverse remodeling and compromising cardiac function (9, 10). The detrimental effects of excessive fibrosis are underscored by its strong association with adverse clinical outcomes, including increased mortality (11, 12). Mass spectrometry–based (MS-based) proteomics

has emerged as a powerful tool to define the ECM composition ("matrisome"), enabling identification and quantitation of ECM proteins of healthy and diseased tissues (13–15). ECM proteomics methods, such as those pioneered by the Lindsey and Mayr laboratories, have been increasingly applied to investigate cardiac matrix biology and its contributions to disease processes (16–20). However, the precise compositional differences of the ECM in failing ICM hearts compared with nonfailing donor hearts remain poorly defined.

To address this knowledge gap, we performed proteomic analysis of left ventricular (LV) apex tissues from patients with end-stage failing ICM (n = 16) and location-matched samples from nonfailing donor hearts free of cardiovascular disease (n = 16). Specifically, we employed sequential protein extraction enabled by photocleavable surfactant 4-hexylphenylazosulfonate (Azo) (21) to enrich ECM proteins (15, 22) for quantitative MS-based proteomic analysis. Our results revealed striking alterations in the ECM composition of the ICM hearts with significant upregulation of critical ECM components, including glycoproteins, proteoglycans, collagens, and ECM regulators. Notably, lysl oxidase-like protein 1 (*LOXL1*), fibulin-1 (*FBLN1*), and versican (*VCAN*), which are closely associated with fibrotic remodeling and ECM cross-linking, were among the most differentially expressed. Functional enrichment analyses uncovered activation of TGFB signaling, integrin-mediated adhesion, and complement pathways, suggesting that these networks may form a self-sustaining loop driving progressive ECM remodeling. Collectively, our findings provide a comprehensive snapshot of ECM remodeling in end-stage failing human ICM hearts and identify promising molecular targets for therapeutic intervention to halt or reverse cardiac ECM remodeling and progression to HF.

Results

Global proteomics analysis of failing ICM and nonfailing donor tissues. To identify differences in the composition of the ECM in failing ICM versus nonfailing donor myocardium, we optimized our cardiac tissue extraction protocol to maximize solubilization of ECM proteins. Our group had previously demonstrated the efficacy of using the photocleavable surfactant, Azo, alone and in combination with a decellularization step using a highly concentrated salt, such as NaCl, in a sequential extraction (15, 22). However, this approach had not been applied to fibrotic, dense muscle tissues, such as human cardiac tissue. Prior studies have reported the improved performance of LiCl over NaCl in the extraction of proteins from muscle tissues (23), and our group has successfully used LiCl to extract myofibrillar proteins from human heart tissue (24). Thus, we employed sequential extractions first with LiCl followed by Azo-containing buffer to effectively decellularize tissue and solubilize ECM proteins.

To gain insight into differences in the composition of the ECM in end-stage ICM, this optimized sequential protein extraction protocol was employed to decellularize tissue and solubilize ECM proteins from the apex of the LV myocardium of failing ICM (n = 16) and nonfailing donor (n = 16) hearts (Figure 1A). The LiCl and Azo extracts (64 total samples; n = 32 ICM, n = 32 control) were subjected to analysis by MS-based proteomics. The total ion chromatograms from each extract across cohorts and normalized intensities following searching demonstrated consistency between biological replicates (Supplemental Figures 1 and 2; supplemental material available online with this article; https://doi.org/10.1172/jci.insight.196933DS1).

For each of the extracts and disease conditions, quantitative reproducibility was assessed by plotting the coefficients of variation (CVs) for the protein-level normalized label-free quantified (LFQ) intensities (Figure 1B). All groups showed median CV values of less than 5%. In addition, normalized LFQ intensities were plotted for each replicate against the others within each of the 4 sample groups and showed an average Pearson's correlation coefficient of r = 0.948. For ICM samples, the average r values for the LiCl and Azo extracts were 0.936 and 0.93, respectively, while for nonfailing controls they were 0.966 and 0.96 (Supplemental Figure 3).

Following database searching of raw mass and tandem mass spectra, data were filtered to retain only genes with 8 or more valid quantified values in at least 1 of the conditions, resulting in the identification of a total of 6,125 unique protein groups across both extracts. After a second filtration step wherein proteins with more than 50% imputed values were removed, 6,118 unique protein groups remained. Overall, more protein groups were quantified in the LiCl extract than the Azo extract, though Azo exhibited a greater degree of overlap between ICM and control donor tissues, suggesting better consistency in detecting shared proteins (Figure 1C). Notably, when comparing the protein intensities across all extracts, we found that major fibrillar proteins, such as type 1 collagen, fibronectin, and elastin, were significantly more abundant in Azo extracts, showing our method effectively enriched insoluble ECM proteins (Supplemental

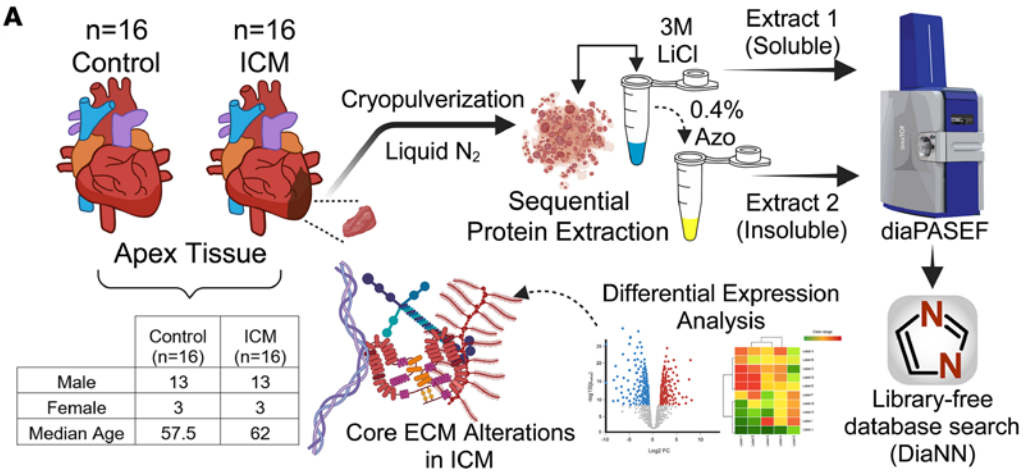

	Control (n=16)	ICM (n=16)
Male	13	13
Female	3	3
Median Age	57.5	62

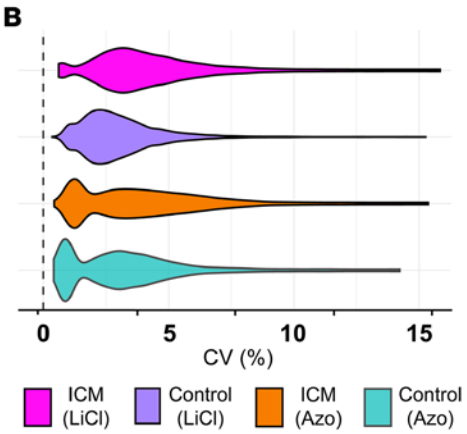

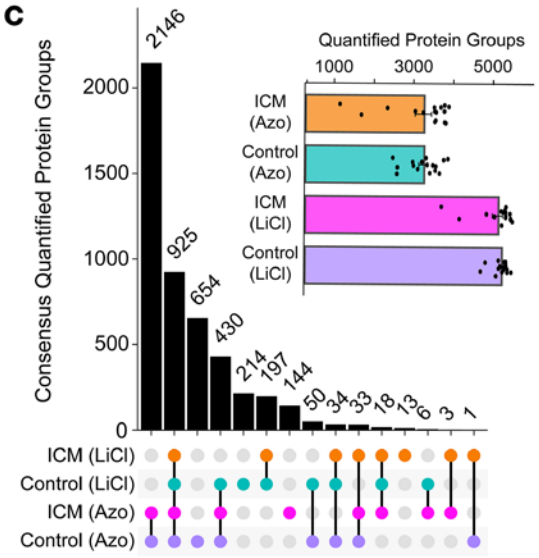

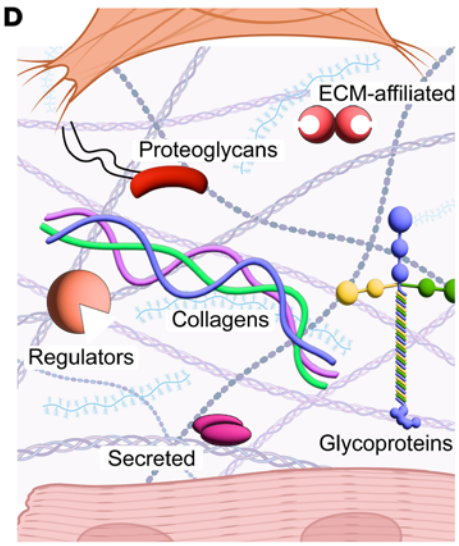

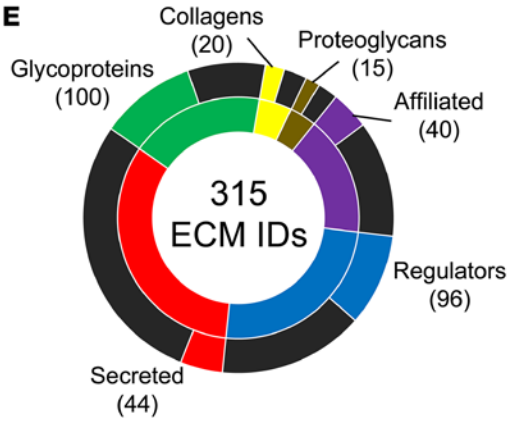

Figure 1. Azo-enabled ECM proteomics method yields reproducible coverage of the matrisome (the collection of proteins in the ECM) in failing ICM and nonfailing donor heart tissues. (**A**) Schematic representation of the workflow for MS-based proteomic analysis of protein extracts from human ICM and donor patient myocardial tissue. Soluble proteins are depleted in the first LiCl extraction (LiCl) followed by solubilization of "insoluble" ECM proteins by extraction with buffer containing the photocleavable surfactant, Azo. (**B**) CVs of protein intensities across extracts from failing ICM and nonfailing donor tissues. The median CV of protein intensities was below 5% for extracts from both groups, indicating high quantitative reproducibility. CVs were calculated by (SD/mean intensity) × 100% for each quantified value in each replicate. (**C**) Upset plot and bar graph (inset) showing more than 6,000 unique protein identifications overall, as well as the degree of overlap between groups. (**D** and **E**) Simplified depiction of major categories of ECM proteins (per MatrisomeDB, ref. 25) (**D**) and breakdown of the number of proteins in each category identified in this study (**E**). The inner circle shows the total number of proteins in each category while the outer circle indicates those that were identified herein. Black segments correspond to proteins present in MatrisomeDB (25) that were not identified in human ICM and donor myocardial tissue.

Figure 4). To assess the effectiveness of ECM extraction, the total number of ECM proteins in all extracts was identified according to information in MatrisomeDB (25) and plotted according to their category. These categories consist of collagens, proteoglycans, glycoproteins, ECM regulators, secreted proteins, and ECM-affiliated proteins (Figure 1D). These results demonstrated that our method was effective at extracting all categories of ECM proteins, with particularly high coverage of glycoproteins, of which our dataset captured approximately 55% of those in the database (Figure 1E).

Alterations in failing human ICM myocardium revealed by global proteomics. Principal component analysis (PCA) of the Azo extract showed clear separation between failing ICM and nonfailing donor samples along PC1, which accounted for 33.34% of the total variance (Figure 2A). Similar clustering by condition was observed in the PCA results of the LiCl extract, though the separation explained a smaller proportion of the variance (Supplemental Figure 5). In general, ICM samples had less cohesion in PCA clustering, which alongside lower Pearson's correlation coefficients can be explained by the relatively higher degree of heterogeneity in the ICM tissues compared with controls. This can likely be explained by differences in factors such as prior MI status, treatments, and comorbid conditions like diabetes (Supplemental Table 1). Differential expression analysis was performed by a limma test, yielding 313 differentially expressed protein groups in the Azo extract (of 2,489 quantified protein groups) and 826 differentially expressed protein groups in LiCl. These were sorted in descending order of adjusted *P* value, and then the top 300 results were plotted in a hierarchical heatmap and clustered by k-means, revealing a distinct pattern in protein abundance in failing ICM compared with nonfailing donor myocardium (Figure 2B).

Differentially expressed proteins broadly clustered into 2 groups: those that were up- and those that were downregulated in failing ICM samples relative to nonfailing controls. Gene Ontology (GO) analysis was performed for differentially expressed proteins, and the GO terms, associated proteins, enrichment strength, and false discovery rate (FDR) are reported in Supplemental Table 4. GO analysis of the 225 proteins upregulated in failing ICM versus nonfailing donor myocardium showed unambiguous association with the ECM (GO:0031012; FDR = 2.83×10^{-43}) and its functions, including ECM organization (GO:0030198; FDR = 2.51×10^{-18}), wound healing (GO:0042060; FDR = 4.59×10^{-12}), and regulation of complement activation (GO:0030449; FDR = 1.68×10^{-10}). Other enriched terms were related to blood coagulation (GO:0007596; 9.83×10^{-11}), platelet degranulation (GO:0002576; FDR = 3.9×10^{-11}), proteolysis (negative regulation of endopeptidase activity; GO:0010951; 6.92×10^{-10}), and cell adhesion (GO:0007155; FDR = 1.47×10^{-5}). The 86 downregulated proteins were associated with the mitochondrion (GO:0005739; FDR = 5.48×10^{-11}) and oxidative phosphorylation (GO:0006119; FDR = 1.51×10^{-9}), underscoring the established link between mitochondrial dysfunction and HF (3, 26) (Figure 2C). GO analysis from the LiCl extract exhibited nearly identical trends, with more terms related to cytosolic proteins attributable to the role of this step in decellularization of tissues (Supplemental Figure 6).

Cardiac ECM remodeling in end-stage HF from ICM. Global proteomics results showed that many of the detected ECM proteins (68 out of the total 315 ECM proteins detected) were upregulated in failing ICM compared with nonfailing donor heart tissue. We contextualized these findings using information in MatrisomeDB (25) to outline categories by which to observe matrisome changes in ICM. In total, 315 ECM proteins were identified from the raw data search, which reduced to 286 after all filtering steps, consisting of 89 glycoproteins (46.6% of database), 18 collagens (40%), 14 proteoglycans (38.9%), 37 ECM-affiliated proteins (22.9%), 87 ECM regulators (35%), and 41 secreted proteins (12.4%). To visualize the categorical ECM differences in ICM compared with control hearts, we plotted the quantile function (0.95% confidence interval) of the $\log_2$ fold changes of differentially expressed ECM proteins across each matrisome category (Figure 3A). Categories that were considered significantly upregulated in failing ICM versus nonfailing control tissues had a mean fold change (± the confidence interval) greater than 0, indicating that glycoproteins (*P* value = 5.23×10^{-11}), ECM regulators (*P* value = 2.29×10^{-5}), proteoglycans (*P* value = 1.62×10^{-5}), and collagens (*P* value = 4.02×10^{-5}) showed significantly higher abundance in Azo of the ICM samples categorically. The same categories were significant in LiCl with the exceptions of ECM-affiliated proteins and collagens, the latter of which we can assume is attributable to increased collagen solubilization by the Azo surfactant. Table 1 summarizes the *P* values and $\log_2$ fold changes for several categories of ECM proteins significantly upregulated in the failing ICM versus nonfailing control myocardium based on the Azo data. These categories, though broadly altered, are functionally heterogeneous, so subsequent sections will highlight individual proteins to provide more detailed interpretation of these changes. The individual proteins from the table are plotted in categories as box plots showing individual replicates in Supplemental Figures 7–10.

Plotting the $\log_2$ fold changes and adjusted *P* values (with thresholds of 0.6 and 0.05, respectively) revealed that the collagen and elastin cross-linking enzyme *LOXL1* was the most highly upregulated protein in the failing ICM, with the lowest *P* value (3.57×10^{-31}) and second-largest $\log_2$ fold change (2.60) (Figure 3, B and C). In other disease models including idiopathic pulmonary fibrosis and liver cirrhosis, *LOXL1* was shown to be stimulated by pro-fibrotic TGFB to increase cross-linking, and its knockdown protects from fibrosis and

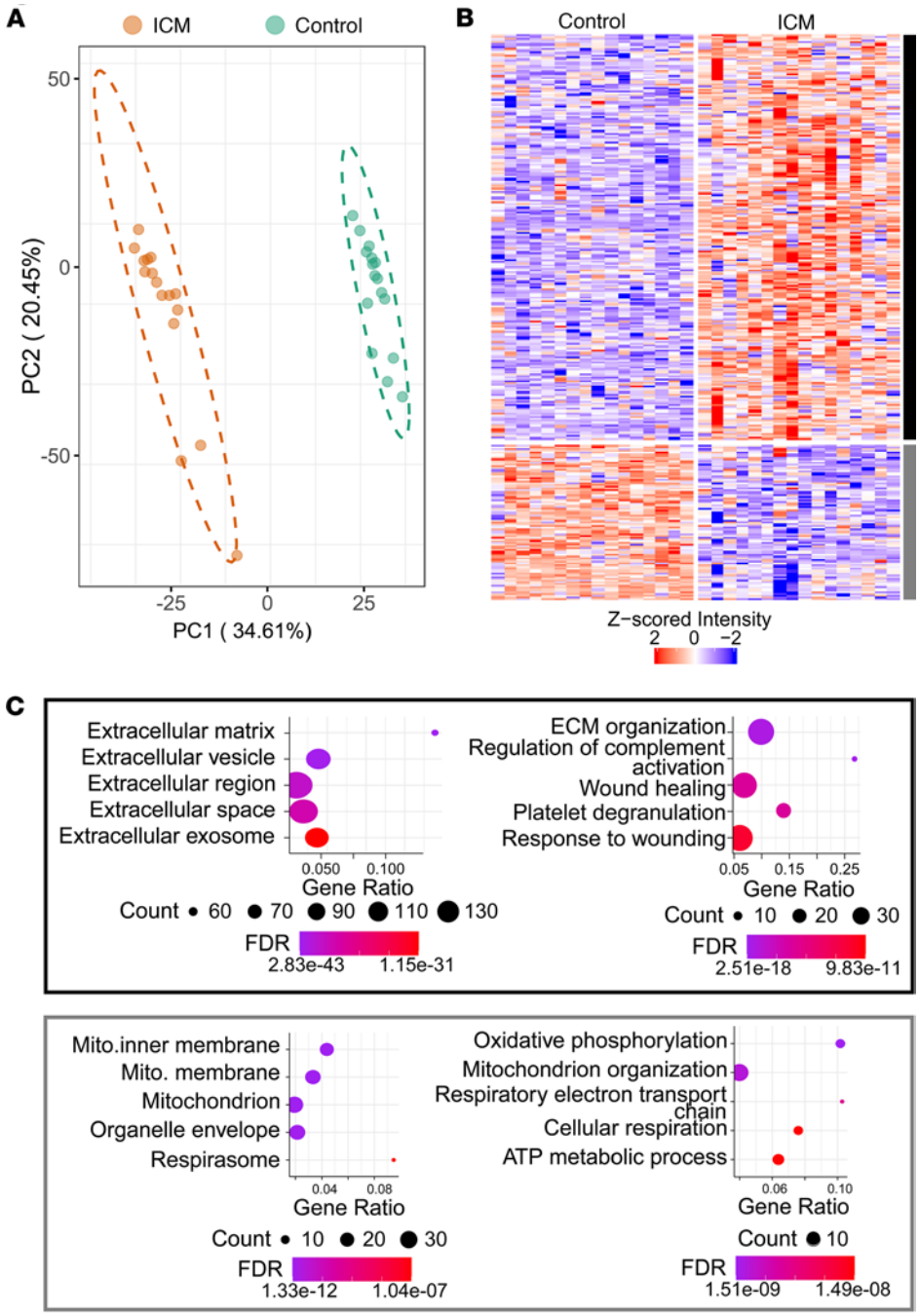

Figure 2. Global proteomics results from ECM-enriched extract reveals alterations in failing ICM versus nonfailing donor myocardium. (**A**) PCA shows clustering and clear separation of failing ICM and nonfailing donor group replicates. The ellipse represents the 95% confidence interval of the data assuming a multivariate normal distribution. (**B**) Heatmap of *Z*-scored protein intensities (top 300 most significant differentially expressed) shows clusters (k-means) of proteins up- and downregulated in failing ICM versus nonfailing control myocardium. (**C**) Bubble plots showing GO terms enriched among protein clusters up- (black) and downregulated (gray) in end-stage failing ICM compared with nonfailing control. Enriched cellular component terms (left) highlight up- and downregulation of ECM and mitochondrial proteins, respectively, in failing ICM compared with nonfailing control myocardium. Similarly, biological process terms (right) enriched among proteins upregulated in the failing ICM myocardium pertained to ECM organization and complement activation while those enriched among downregulated proteins were concerned with metabolic processes. FDR is *P* value–corrected by the Benjamini-Hochberg method, done automatically by STRING.

reduces expression of pro-fibrotic metalloproteases and collagens (27). The next most significantly upregulated protein based on *P* value was the adhesive ECM glycoprotein *FBLN1* (*P* value = 4.6×10^{-15}), which also had the fourth-highest $\log_2$ fold change overall in the Azo extract (Figure 3, B and C). During cardiac development,

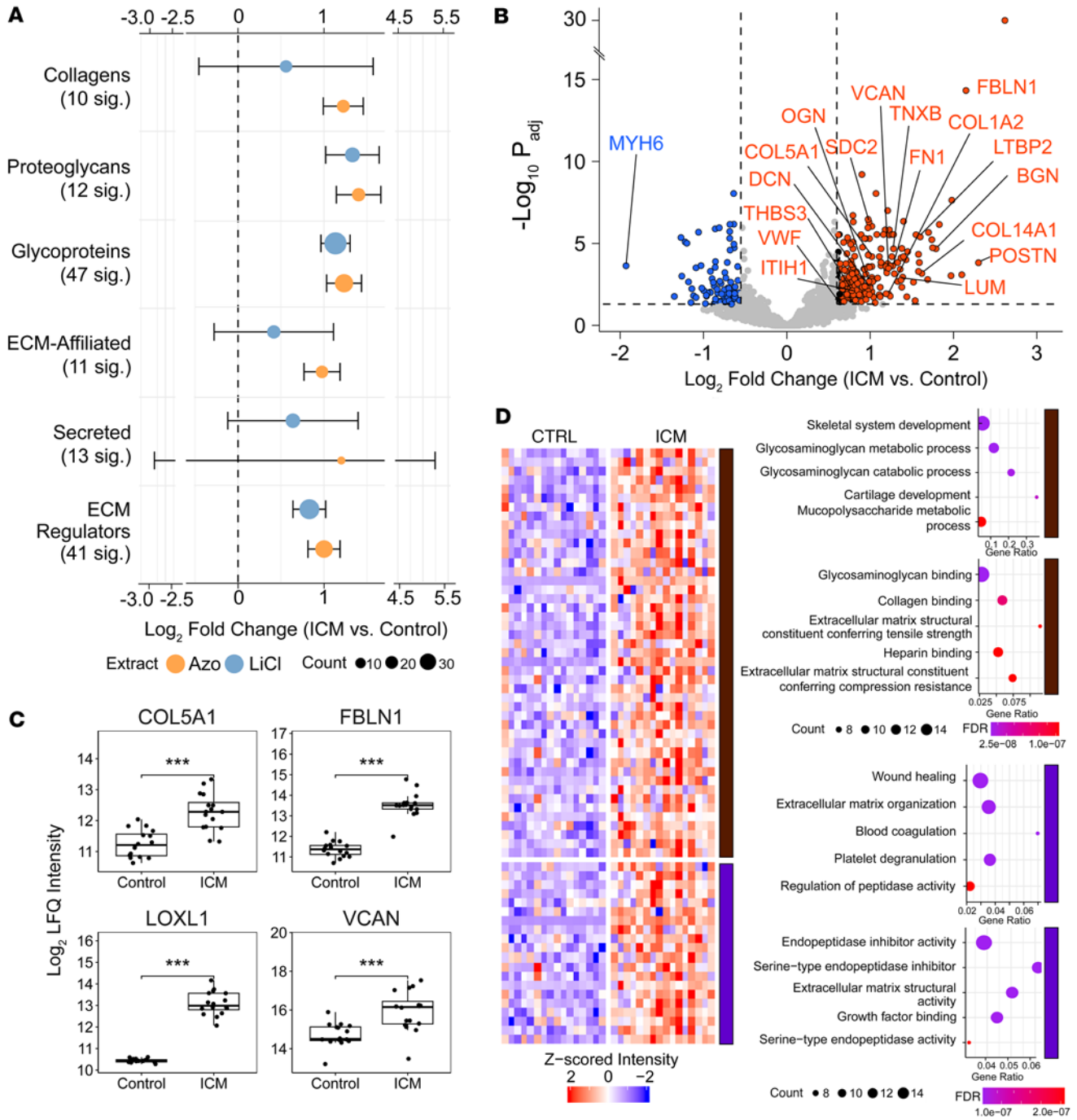

Figure 3. ECM remodeling in end-stage HF from ICM. (**A**) Dot plot showing categorical $\log_2$ fold change in the intensities of matrisome proteins. Mean and SD of $\log_2$ fold changes for all ECM proteins in each extract and category were plotted. Overall, core matrisome proteins (collagens, proteoglycans, and glycoproteins), as well as ECM regulators, were significantly upregulated in failing ICM LV tissue. Means were tested for significance using Student's 2-tailed *t* test, and the 97.5% confidence interval was computed. (**B**) Volcano plot showing select proteins up- and downregulated in failing ICM versus nonfailing donor myocardium. To be considered significant, a log fold change > 0.6 (>1.5-fold) and an adjusted $P < 0.05$ (–log p-adj > 1.3) were both required. (**C**) Core collagens, ECM regulators, glycoproteins, and proteoglycans show increased expression in ICM. Box plots show the interquartile range, median (line), and minimum and maximum (whiskers). Significance testing was performed using limma. Then *P* values were adjusted by independent hypothesis weighting and plotted as follows: *** ≤ 0.001. (**D**) Clustered heatmap and corresponding bubble plots showing the results of GO analysis using the list of ECM proteins upregulated in failing ICM myocardial tissue. In the first cluster, biological processes (top) relate to carbohydrate metabolism with molecular functions (bottom) of binding and matrix structural properties. The second cluster pertains more to matrix regulation by growth factors and peptidases. FDR is *P* value–corrected by the Benjamini-Hochberg method, done automatically by STRING.

FBLN1 promotes ADAMTS-1 (a disintegrin and metalloproteinase with thrombospondin motifs 1) cleavage of chondroitin sulfate proteoglycan *VCAN* (28). *VCAN* accumulation has been previously reported in failing hearts and shown to be reduced upon treatment with beta blockers regulated by ADAMTS family proteins

(18). Consistent with this, we observed significantly higher *VCAN* expression in the failing ICM compared with nonfailing donor tissue (P value = 3.22×10^{-4}) (Figure 3, B and C). These findings suggest that the marked increase in *FBLN1* observed in failing ICM may serve as a protective mechanism, potentially compensating for elevated *VCAN* expression by stimulating ADAMTS-mediated proteolysis.

To further probe the pathways underlying these ECM differences in ICM, we performed hierarchical clustering of the ECM proteins significantly upregulated in failing ICM compared with nonfailing donor myocardium, again with 2 k-means clustering (Figure 3D). In cluster 1 we observed many terms related to glycosaminoglycans (GAGs), including GAG metabolism (GO:0030203; FDR = 6.13×10^{-8}), catabolism (GO:0006027; FDR = 1.05×10^{-7}), and sulfur compound metabolic process (GO:0044273; FDR = 1.44×10^{-6}) relating to GAG sulfation. Of note, there were several terms related to cartilage development (GO:0051216; FDR = 1.05×10^{-7}). Evidence shows similar hierarchical organization and regulation of ECM in both heart and cartilaginous connective tissues, including regulatory pathways involving aggrecan (*ACAN*) and tenascins (*TNC* and *TNXB*), which we found were significantly upregulated in ICM tissues (29, 30). The GO functional enrichment analysis returned terms primarily related to binding — collagen binding (GO:0005518; FDR = 1.26×10^{-9}), GAG binding (GO:0005539; FDR = 1.33×10^{-12}), integrin binding (GO:0005178; FDR = 1.40×10^{-4}), ECM binding (GO:0050840; FDR = 1.30×10^{-3}), and calcium ion binding (GO:0005509; FDR = 2.32×10^{-6}) — but also had terms related to specific matrix structural elements. ECM structural constituents conferring tensile strength (i.e., resistance to stretching) were all collagens (*COL1A2*, *COL3A1*, *COL6A2*, *COL6A3*, *COL12A1*, *COL14A1*; GO:0030020; FDR = 2.93×10^{-8}), while those conferring compression resistance were proteoglycans (*DCN*, *VCAN*, *LUM*, *BGN*, *PRELP*; GO:0030021; FDR = 1.28×10^{-7}). Cluster 2 terms overlapped greatly with the generally upregulated protein groups, with major categories such as coagulation (e.g., negative regulation of blood coagulation; GO:0030195; FDR = 4.66×10^{-6}) and proteolysis (GO:0052547; FDR = 2.86×10^{-7}). Functional terms make it clear these trends relate to the SERPIN family of serine protease inhibitors (GO:0004867; FDR = 8.18×10^{-6}) and matrix metalloproteinases, *MMP9* in particular. Growth factor signaling also appeared as an enriched term, which is consistent with the role of TGFB in promoting ECM remodeling and fibrosis in ICM (31, 32).

Pathway analysis revealed TGFB signaling drives ECM remodeling in end-stage ICM. We next performed functional annotation clustering using Database for Annotation, Visualization and Integrated Discovery (DAVID) (33) to group similar annotations and clarify broader trends in the differentially expressed proteins in ICM tissues (Supplemental Table 4). Clusters were ranked by enrichment score, a geometric mean of P values for terms within a cluster, and using the differentially expressed proteins in the Azo extract, we observed 20 clusters wherein the top term's Benjamini-Hochberg–adjusted P value was significant (<0.05). The top 2 clusters (enrichment scores = 22.77 and 16.19) unsurprisingly contained Kyoto Encyclopedia of Genes and Genomes (KEGG) and GO terms relating to ECM components, though the second more generically related to ECM components and the first had annotations of secreted proteins and glycoproteins. The next highest clusters were related to blood coagulation (enrichment score = 6.13), cell adhesion (5.12), calcium-binding epidermal growth factor domains (3.49), and SERPINs (3.48). Clusters 9 and 10 reflected complement pathways/innate immunity (2.97) and immunoglobulin binding (2.92), and cluster 12 reflected small leucine-rich proteoglycans (SLRPs), such as *DCN*, *LUM*, *BGN*, and *PRELP* (2.58).

To provide the context of protein-protein interactions into the pathway analyses, we used the R package pathfindR (34) to perform an active subnetwork search in a protein interaction network, then performed pathway enrichment using these networks. A P value threshold of 0.05 was used for significance, and active subnetwork search was iterated 10 times, with the lowest P value among iterations used to determine the overall significance of the term. Using KEGG annotations, 51 terms were significantly enriched from Azo using this approach, and the terms with the largest fold changes were complement and coagulation cascades (lowest P value = 1.06×10^{-21}), oxidative phosphorylation (P value = 3.04×10^{-26}), cardiac muscle contraction (P value = 3.87×10^{-10}), and ECM-receptor interaction (P value = 3.28×10^{-11}) (Figure 4A).

From GO terms (using all terms from cellular component, biological process, and molecular function), 92 entries were deemed significant. Significant GO terms were largely in agreement with the previous GO results, though the fold enrichment provided for each term provided new context for particularly large changes, including the 61-fold enrichment for ECM structural constituents conferring compression resistance (P value = 2.38×10^{-2}), a category containing mainly small leucine-rich proteoglycans. Notably, integrin activation (P value = 2.72×10^{-5}) and integrin-mediated signaling pathways (P value = 3.39×10^{-5}) were also significant, displaying a 24-fold and a 10-fold enrichment, respectively. Hierarchical clustering of

Table 1. Proteins significantly upregulated in the Azo extract from failing ICM versus nonfailing donor hearts

Regulators			Collagens			Glycoproteins			Proteoglycans		
Gene	*P* value	LFC	Gene	*P* value	LFC	Gene	*P* value	LFC	Gene	*P* value	LFC
A2M	4.47E-03	0.91	COL12A1	9.88E-05	1.43	FN1	2.37E-04	1.27	ASPN	1.59E-03	1.69
ADAMTSL4	5.23E-03	0.80	COL14A1	6.74E-04	1.62	FGB	4.72E-03	1.12	BGN	2.10E-05	1.79
F10	1.57E-03	1.03	COL1A2	1.21E-02	1.22	FGG	3.52E-02	0.90	DCN	5.21E-03	1.00
F7	2.63E-04	0.98	COL3A1	2.09E-03	1.33	TNC	4.67E-03	1.38	HAPLN1	4.58E-05	1.58
HTRA1	1.18E-03	1.02	COL5A1	6.39E-05	1.02	FGA	1.13E-03	1.39	LUM	1.72E-03	1.37
HTRA3	1.92E-03	0.72	COL6A2	8.68E-03	1.02	AEBP1	5.90E-06	1.74	OGN	2.04E-03	0.99
ITIH1	1.07E-02	0.82	COL6A3	7.67E-03	0.93	EFEMP1	2.57E-04	1.22	PRELP	1.45E-04	1.59
ITIH2	2.80E-03	0.73				POSTN	1.50E-04	2.30	VCAN	3.22E-04	1.22
ITIH3	2.84E-06	1.08				TNXB	2.10E-05	1.28			
ITIH4	4.07E-02	0.65				MFGE8	3.84E-03	0.96			
KNG1	4.64E-03	0.91				TGFBI	2.57E-04	1.02			
LOXL1	3.57E-31	2.60				ABI3BP	2.02E-05	1.38			
MMP9	2.67E-02	0.95				FBLN2	1.49E-03	0.87			
P4HA2	4.20E-05	0.72				FBLN1	4.60E-15	2.15			
SERPINA5	3.82E-04	0.93				LTBP2	3.96E-06	1.60			
SERPIND1	4.24E-03	0.94				VWF	3.13E-02	0.61			
SERPINE2	2.55E-04	1.19				LTBP3	3.55E-04	0.93			
SERPINF1	1.50E-02	0.88				LTBP4	8.57E-03	0.82			
SERPING1	3.13E-05	1.45				MGP	1.82E-05	1.75			
SERPINH1	4.69E-02	0.72				FBLN5	1.37E-02	0.81			
TGM2	1.31E-02	0.99				IGFALS	2.29E-08	1.98			
						EFEMP2	9.82E-03	0.73			
						PAPLN	1.32E-02	0.62			
						THBS3	7.54E-03	0.78			

limma was used to calculate *P* values, and the shown value is the adjusted *P* value after independent hypothesis weighting using peptide count as the covariate. Adjusted *P* value < 0.05 was considered statistically significant. A positive log fold change (LFC) indicates upregulation in ICM.

the enriched terms linked ECM organization to integrin binding (Supplemental Figure 11), and plotting individual proteins showed *FN1*, *APOE*, and *EFEMP2* linked those terms as well as endoplasmic reticulum lumen, heparin binding, and peptide cross-linking (Supplemental Figure 12).

Reactome searches yielded 134 significant terms, of which the majority with the lowest *P* values were related to inflammation, hemostasis, and dysregulated electron transport. Insulin-like growth factor binding was previously shown as a significant term from GO analyses, and a similar Reactome annotation, Regulation of Insulin-like Growth Factor (IGF) transport and uptake by Insulin-like Growth Factor Binding Proteins (IGFBPs), provided a more specific description of the pathway with an expanded list of relevant proteins. Hierarchical clustering showed multiple distinct groups relating to ECM organization, collagen biosynthesis, and ECM degradation (Supplemental Figure 13). In addition, clusters involving syndecan/nonintegrin cell-surface signaling, integrin MAPK signaling, complement cascades, and Toll-like receptor signaling were all enriched. Fibrinogens linked Toll-like receptors and clot formation to ECM signaling, while *FN1* again spanned categories of ECM organization and cell surface signaling by integrins and syndecans (Supplemental Figure 14). LiCl extract analysis displayed the same ECM-related terms as in Azo but also captured TGFB signaling (P value = 2.2×10^{-2}). Plotting relevant ECM-related terms, there was clearly a substantial degree of overlap between TGFB signaling and ECM proteins involved in processes of extracellular structure and cellular adhesion (Figure 4B). In particular, *THBS1*, *FN1*, and *COL1A2* appeared to be focal points connecting these processes (Figure 4B).

Bidirectional ECM/myocyte signaling in ICM. The bidirectional nature of ECM signaling with cells indicates that its composition likely plays a greater role in disease progression beyond deposition following injury and cardiomyocyte death. In ICM, the mechanical properties of ECM are altered (35–37), which may enhance pro-fibrotic TGFB signaling and further drive fibrosis progression. This concept is supported by studies showing that engineered heart tissues derived from stem cells grown on ECM from hypertrophic hearts exhibited contractile dysfunction (38). Consistent with these findings, our data reveal

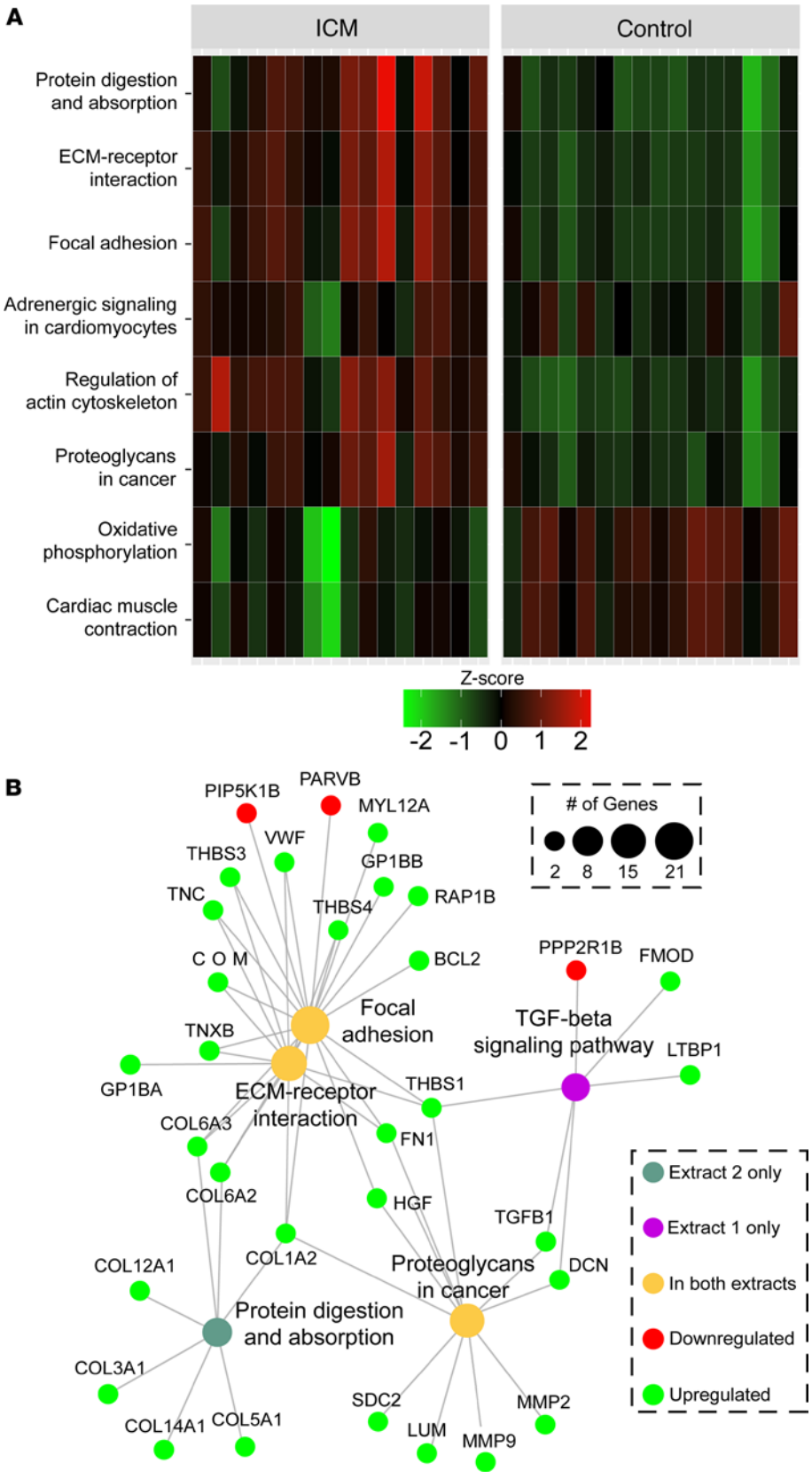

Figure 4. Pathway analysis implicates the TGFB signaling network in altered ECM composition in the myocardium of individuals with end-stage failing ICM. (**A**) Heatmap of agglomerated *Z*-scores for KEGG pathway terms across samples showing upregulation of pathways related to focal adhesions and ECM-receptor interactions. In addition, these changes are accompanied by increased regulation of the cytoskeleton and decreased expression of metabolic and contractile proteins. Term changes are visualized for the ECM-enriched extract. (**B**) Term-protein network generated using input data from both extracts demonstrates connections between pathways via specific proteins. In general, adhesive glycoproteins (thrombospondins, tenascins, fibronectin, vitronectin) and proteoglycans (decorin) connect receptor processes to focal adhesion and regulation by protein digestion and TGFB pathways.

alterations in both the ECM and the contractile machinery of cardiomyocytes. Figure 5A shows a schematic of the connective proteins linking ECM to internal contractile machinery via costameres (39), and Figure 5B shows the significant proteins in our experiment corresponding to these linkages. Costameres are similar to the focal adhesions cardiomyocytes have at their distal ends but connect laterally to form

sarcolemmal-cytoskeletal attachments (35, 39). In addition, costameric proteins shown to interact with integrins such as kindlins (*FERMT2/3*) and parvins also significantly change at end-stage ICM. *FERMT2* (also known as kindlin-2) is an essential component of vertebrate intercalated discs and is essential for cytoskeletal organization and membrane attachment during development (40).

We observed a significant downregulation of kindlin-2 in ICM, consistent with previous studies in mice showing that deletion of this gene results in HF and premature death (41). Interestingly, loss of *FERMT2* was contrasted by upregulation of *FERMT3* and *ITGB2*, both of which are exclusively expressed in hematopoietic cells. The interaction of *FERMT3*/*ITGB2* is particularly important in platelet aggregation and innate immune response (42, 43) and is associated with unstable atherosclerotic plaques (44). We also observed the significant downregulation of muscle-specific integrin-binding protein melusin (*ITGB1BP2*), which protects the heart during ischemic injury via integrin-dependent activation of PI3K/AKT and ERK pathways (45). Figure 5C shows the specific proteins that changed at the interconnected stages of ECM, costamere/sarcolemma, and sarcomere. These include the adhesive glycoproteins like fibronectin, thrombospondins, and tenascins, which all increased in ICM, and components of the costamere like kindlins, parvins, and melusin. Intracellularly, myosin heavy chain 6 greatly decreased, as did tropomyosin-2 and myomesin-2, while myosin heavy chain 10 increased. Overall, there was a trend toward decreased expression of the intracellular components relative to the extracellular proteins. It is likely this is attributable at least in part to replacement fibrosis — cell death decreases the relative expression of intracellular components as ECM deposition takes the place of cells. Despite these contributions, interstitial fibrosis resulting in intracellular change is also very likely, given most patients in this study had no history of MI and had only experienced chronic ischemia.

Discussion

Myocardial ischemia triggers the activation of cardiac fibroblasts stimulated by mechanical forces, growth factors, and cytokines to remodel the myocardium (9, 10, 46). Differentiation of these cells to myofibroblasts leads to pathological remodeling of myocardial ECM and subsequent cardiac fibrosis — key processes in the progression of ischemia to ICM and eventual HF (8, 46). To identify differences in the composition of the ECM in end-stage failing ICM hearts versus nonfailing controls, we employed a sequential extraction to achieve maximal depth of coverage and focused primarily on analysis of the second extract, which relied on a photocleavable surfactant, Azo (21, 47), to solubilize core ECM proteins for analysis and quantitation by MS-based proteomics. For this study we compared differential protein abundance from 16 failing ICM tissues obtained during left ventricular assist device (LVAD) implantation with those from 16 region-matched nonfailing donors without a history of cardiovascular disease. Previous proteomics studies of human cardiac tissues have focused on nonischemic disease (48) or on the effect of LVAD implantation by using patient-matched pre- and postoperative samples (49).

At its core, the ECM is composed of fibrous proteins such as collagens, fibronectins, and laminins; proteoglycans, which consist of core proteins covalently bound to GAG chains; secreted factors (e.g., S100 proteins); matrix regulators (e.g., matrix metalloproteinases); and matricellular proteins (e.g., thrombospondins) (6, 7, 11, 12, 16, 50, 51). Structural components of the cardiac ECM primarily include collagens (types I and III and to a lesser extent IV, V, and VI), elastin, and fibronectin, whereas nonstructural ECM is largely composed of glycosylated proteins including both proteoglycans and glycoproteins and of glycosaminoglycans such as hyaluronan, heparan sulfate, and chondroitin sulfate (50, 52). Beyond fibrillar components, cardiac ECM also includes glycoproteins like fibronectin, proteoglycans, GAGs, matricellular proteins, proteases, and growth factors.

Given the inherent challenges in solubilizing ECM proteins owing to their insolubility, extensive cross-linking, and structural complexity, efforts have been dedicated to developing specialized extraction methods to extract the ECM proteins from heart tissues (16, 19, 20). For example, Barallobre-Barreiro et al. utilized sequential extraction with 0.5 mol/L NaCl, 0.1% SDS, and 4 mol/L guanidine-HCl to decellularize and sequentially extract ECM proteins, enabling the identification and analysis of 139 ECM proteins from the porcine myocardium subjected to ischemia/reperfusion injury (16). Similarly, de Castro Brás et al. developed the Texas 3-step decellularization protocol, which sequentially uses salt, detergent, and chaotropic agents to enrich for ECM components in cardiac tissue, facilitating proteomic analysis of the cardiac ECM (19). In this study, we used sequential extraction with the photocleavable surfactant, Azo, allowing fast tissue decellularization and efficient extraction and enrichment of ECM proteins, which dramatically

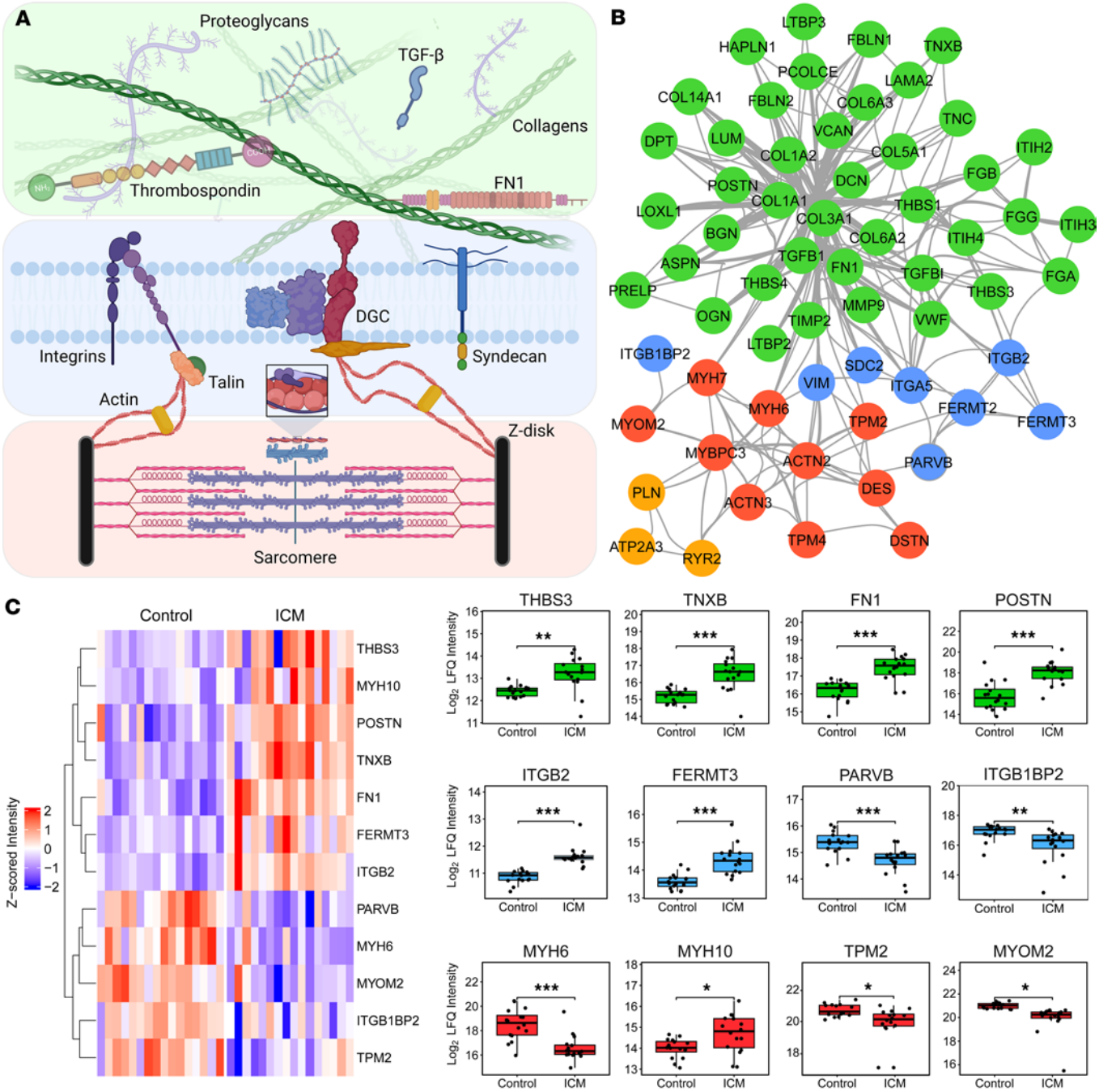

Figure 5. Bidirectional communication between ECM and cardiomyocytes contributes to ICM. (**A**) A general scheme for interaction between ECM and cardiomyocyte contractile machinery is shown. At the sarcolemma, integrins and other costameric proteins transmit forces from ECM to cytoskeleton and then to sarcomere. DGC, dystrophin glycoprotein complex. (**B**) Depiction of significantly altered protein groups from our data and the corresponding protein-protein interactions plotted in Cytoscape (93). (**C**) Heatmap and box plots of specific protein groups, demonstrating increased expression of ECM consistent with fibrosis and changes to intracellular components of cardiomyocytes, including fermitins, actinins, and myosin heavy-chain isoforms. For the box plots, ITGB2, FERMT3, MYH6, and MYH10 are plotted from the Azo extract, while PARVB, ITGB1BP2, TPM2, and MYOM2 are plotted from the LiCl extract. Box plots show the interquartile range, median (line), and minimum and maximum (whiskers). Significance testing was performed using limma. Then *P* values were adjusted by independent hypothesis weighting and plotted as follows: * ≤ 0.05, ** ≤ 0.01, *** ≤ 0.001.

expanded the coverage of ECM proteins and permitted the analysis of more than 315 ECM proteins from human failing ICM and nonfailing donor hearts. Our method has shown high reproducibility for label-free quantification and enabled the identification of significantly altered proteins in the myocardium of patients with end-stage ICM in comparison with the controls.

The most significantly differentially expressed protein in our data was the elastin and collagen cross-linking protein *LOXL1* (adjusted *P* value = 3.57×10^{-31}; $\log_2$ fold change = 2.6). *LOXL1* was quantified in 12/16 ICM tissue samples using the Azo-based extraction and was absent in all nonfailing control samples, indicating a marked upregulation in failing hearts. Although its absolute intensity was relatively low, the detection and quantification of *LOXL1* underscore the importance of our extraction method in capturing low-abundance proteins that may play vital roles in pathological remodeling. In animal models of hepatic and pulmonary fibrosis, *LOXL1* has been shown to regulate TGFB-induced fibrosis, and its knockdown inhibits fibrotic proliferation and reduces expression of type I collagens and pro-fibrotic metalloproteinases (27). The substantial increase in *LOXL1* observed in this study suggests a previously underappreciated role of this enzyme for myocardial stiffening and subsequent LV dysfunction in end-stage ICM, potentially through elastin cross-linking. Additionally, *LOXL1* may contribute to collagen cross-linking, a process associated with increased myocardial interstitial fibrosis (MIF) and adverse clinical outcomes (53, 54).

We also observed a significant increase in the gelatinase *MMP9* (adjusted *P* value = 0.026, $\log_2$ fold change = 0.951) though to a lesser extent than *LOXL1*. *MMP9* is known to degrade type I collagen fibers, and the greater relative increase in cross-linking enzyme lends credence to the idea that MIF in HF involves cross-linking predominating over matrix degradation (53). Alongside these changes, several tissue inhibitors of metalloproteinases and inter-alpha-trypsin inhibitors were significantly upregulated in ICM tissues (Table 1). These proteins regulate ECM deposition by inhibiting degradation by metalloproteinases, and it is likely that the imbalanced expression of the proteases and their inhibitors contributes to the transition from ischemia to HF (12, 55).

Alongside cross-linking, collagen fiber composition and alignment vis-à-vis cardiomyocytes both affect the mechanical dysfunction of cardiac tissue in ICM (56–59). We observed an increased abundance of types I/III collagens and the expected decrease in I:III ratio associated with ICM, which is consistent with a previous report (57). Elevation of these fibrillar collagens contributes significantly to cardiac fibrosis and can activate cardiac fibroblasts to create feedback loops of ECM deposition (60, 61). Collagens I and III drive proliferation of undifferentiated cardiac fibroblasts whereas collagen VI (*COL6A2*, adjusted *P* value = 0.0086, $\log_2$ fold change = 1.02; *COL6A3*, adjusted *P* value = 0.0076, $\log_2$ fold change = 0.932) potently induces myofibroblast differentiation (62). Mouse knockout of collagen VI promotes healing and reduces fibrosis, seemingly because of rapid myofibroblast apoptosis, which prevents excessive matrix deposition (63). We also observed significant increases to the SLRPs asporin (*ASPN*), biglycan (*BGN*), decorin (*DCN*), lumican (*LUM*), and mimecan (*OGN*), which is known to bind collagens and regulate fibrillogenesis (64). SLRPs generally modulate collagen fibril formation and thus ECM integrity, tensile strength, and organization. In a mouse model of ICM, *ASPN* was one of the top differentially expressed genes and exhibited an antifibrotic effect by attenuating TGFB signaling (65). *DCN* is also antifibrotic, slowing the rate of fibrillogenesis and blocking TGFB-induced collagen deposition in 3-dimensional collagen matrices (66). Contrary to this, *LUM* induces collagen I expression, as well as matrix-remodeling molecules, such as *LOX*, *TGFB*, and *MMP9* (51). Further efforts into the posttranslational modifications of SLRPs, including both N-linked glycosylation and GAG chain composition/sulfation, are needed to elucidate their specific roles in ICM and HF.

TGFB signaling is the central mediator of postinfarction cardiac repair; however, by stimulating ECM preservation and myofibroblast differentiation/activation, it also serves as a key contributor to fibrotic remodeling (32). Previous proteomics analysis of ECM in a porcine ischemia/reperfusion model identified a central role for *TGFB1* signaling in orchestrating early- and late-stage ECM remodeling (16). We observed significant increases in *TGFB1* and TGFB-related proteins, including latent transforming growth factor binding proteins (*LTBP1/3/4*), which are known to play a critical role in the maintenance, extracellular secretion, and integrin-mediated activation of TGFB (67). We also noted a decreased abundance of *SMAD1*, a molecule downstream of TGFB activation, which has a documented antiapoptotic effect in cardiomyocytes (68). The fine detail of how ECM composition influences TGFB activation remains unclear, but it is known that mechanical stiffening and fibrosis lower the activation threshold for TGFB (69). The different isoforms of LTBPs show different matrix-binding preferences; for example, *LTBP1* mainly interacts with fibronectin, mediated by heparan sulfate proteoglycans, and *LTBP3/4* bind fibulins (69). Our experiment showed increased abundance of fibronectin and fibulins in failing ICM hearts, alongside other proteins that mediate the interaction between latent TGFB and the ECM like small leucine-rich proteoglycans and integrins. These findings also support a TGFB-driven feedback loop, in which ECM stiffening enhances mechanosensitive TGFB, which in turn promotes further ECM deposition and mechanical

remodeling of the matrix properties (69, 70). Additional regulatory inputs, such as the renin-angiotensin-aldosterone system, further contribute to fibroblast activation and subsequent ECM deposition by stimulating TGFB and related pathways (71). Beyond mechanical and systemic regulation, paracrine signaling by secretion of matricellular proteins is pivotal in mediating interactions between ECM and cells (35).

In our experiment, we observed significant changes to adhesive glycoproteins and matricellular proteins in end-stage failing ICM hearts, including tenascins (*TNC* and *TNXB*), thrombospondins (*THBS1/3/4*), periostin (*POSTN*), and von Willebrand factor (*VWF*). Thrombospondin-1 is directly involved in TGFB activation by forming an interaction with the TGFB propeptide preventing formation of latent complexes, which increases the amount of the mature protein that can bind to receptors (72). Thrombospondins 1, 2, and 4 are known to play protective roles in the progression of cardiac diseases and have been explored as therapeutic targets (73). Recent mouse studies revealed that increased abundance of *THBS3* reduces sarcolemmal stability by downregulating a variety of integrin subunits, thus enhancing cardiac pathology upon stress (74). It was also shown that its expression was higher in the blood of patients with stable CAD compared with those who had experienced MI (75). For the first time to our knowledge, we have shown that *THBS3* is upregulated significantly in human end-stage ICM (P value = 7.54×10^{-3}), likely contributing to the disease progression in a similar manner. Overall, thrombospondins appear to be key modulators of integrin signaling and cardiac remodeling.

Although there is no standard definition for ICM, it can be considered LV dysfunction occurring with severe CAD and either history of MI or stenosis of >75% of left anterior descending artery/2 or more coronary arteries (5). Improvements in patient survival following MI have resulted in a greater prevalence of ICM-induced HF (76). In spite of this, fewer than half (6/16) of the patients with ICM in our study had a documented MI, with the remainder diagnosed based on the severity of CAD. Even in the absence of MI, chronic ICM still results in profound MIF, though the underlying mechanism and pathophysiology of this outcome are unclear. In fact, Frangogiannis et al. have shown that the extent of interstitial fibrosis distinguishes irreversibly dysfunctional myocardium from tissue capable of functional recovery, suggesting chronic ICM progresses through ongoing fibrotic remodeling (32, 46, 77). Our data implicate TGFB signaling as an important factor in end-stage HF from ICM, though the specific mechanisms of activation remain to be investigated. Previous studies suggested that acidity or hypoxia-induced signaling may contribute to TGFB activation in ICM (31), and it is likely that the underlying cause of disease progression is dysregulation of TGFB signaling itself. For example, we found *SMAD1*, a cytosolic protein that is phosphorylated in the canonical TGFB pathway that protects against apoptosis in ischemia/reperfusion injury models (68), is downregulated in ICM tissues (78). There are ultimately many mechanisms that activate latent TGFB, including the aforementioned *THBS1* (72), extracellular proteases (79), and mechanical strain (69). A feedback loop occurs in fibrosis when sufficiently stiff ECM reduces the threshold for TGFB activation, which in turn results in myofibroblast activation and more ECM deposition (69, 80). Our data suggest this process is possibly occurring in ICM, as we observe significant increases to both structural ECM components and many TGFB-related proteins in end-stage ICM tissues. Further studies are needed to elucidate how chronic ischemia drives myocardial matrix remodeling and interacts with dysregulated TGFB signaling.

Overall, we have conducted a quantitative proteomics experiment to analyze the molecular changes, particularly in the ECM, of heart tissues from patients in end-stage HF from ICM. Our study revealed the drastic changes to ECM deposition in the ICM heart, including increased abundance of adhesive glycoproteins, matricellular proteins, and small leucine-rich proteoglycans. Notably, we found that *THBS3* is significantly increased in ICM tissues and likely contributes to disease progression by destabilizing sarcolemmal integrin levels. This is consistent with our findings showing the dramatic increase in cross-linking protein *LOXL1*, suggesting altered mechanical properties of the matrix. Together, these findings point to a pathological interplay between TGFB signaling and mechanosignaling via integrins as drivers of contractile dysfunction in the end stage of ischemic disease. Altered protein expression at costameres, including integrins and their intracellular signaling partners, such as kindlins and melusin, may further exacerbate the deleterious effects of increased fibrosis on cardiac function.

Although we believe these findings are novel, an inherent limitation to this discovery-based proteomics study is that it remains largely descriptive, and further mechanistic study is needed to validate the roles of ECM proteins in ischemic disease. Another limitation of our study is comparing ICM samples to only nonfailing hearts. Inclusion of other types of cardiomyopathies in the future would help identify ICM-specific ECM molecular signatures. Additionally, the use of relatively small portions of LV tissue, collected from

the apex during LVAD implantation, may not fully capture the extent of cardiac remodeling in ICM and thus may be susceptible to the effects of regional heterogeneity. Furthermore, the unequal representation of male and female individuals in diseased tissues may influence the interpretation of the results, especially given the sex-specific nature of cardiac fibrosis (81, 82). Future studies should more systematically evaluate the pathobiology of ischemic disease and cardiac fibrosis in a sex-specific manner. Methodologically, although multistep sequential extractions are widely used in ECM proteomics (13, 15, 19, 20, 22), they may complicate quantification because of overlap of proteins across fractions. Our group has recently reported a single-step extraction yields comparable results to 2-step protocols, offering a potentially improved approach for future ECM quantification (83). Improved mechanistic insight and ECM coverage could be achieved in further studies by including analysis of common ECM posttranslational modifications, such as hydroxylation of proline and glycosylation, both of which have functional consequences associated with disease progression (50, 84). Further investigation is needed to understand the origin of TGFB dysregulation and its role in fibrosis and their causal linkages to ischemia. Our data also revealed large-scale reduction in oxidative metabolism, and it would be prudent to investigate links between the metabolic phenotype of cardiomyocytes in ICM and the progression of interstitial fibrosis.

Methods

Sex as a biological variable. In this study, samples were used from both men and women. Of the nonfailing donor hearts, half (n = 8) were from women and half were from men. For ICM hearts, 3 were from women and 13 from men. Sex was not considered as a variable because of the relative overrepresentation of males in our ICM samples, but sex was considered as a potential contributing factor toward any outliers or incongruent values.

Chemicals and reagents. Trypsin Gold, Mass Spectrometry Grade, was purchased from Promega (catalog V5280). The photocleavable surfactant Azo was purchased from MilliporeSigma (catalog 919233). Solutions were prepared in HPLC-grade water from Thermo Fisher Scientific. Amicon Ultra Centrifugal Filter, 10 kDa MWCO filters were purchased from MilliporeSigma (catalog UFC5010). All other reagents and buffers were purchased from Thermo Fisher Scientific or MilliporeSigma unless otherwise noted.

Human cardiac tissue collection. Available clinical data, including age, sex, cause of death, and medical history, are listed for the heart tissues used in this study in Supplemental Table 1. Tissue from the apex of the left ventricles of failing ICM and nonfailing donor hearts (n = 16 each) was used for the experiments described in this study. Tissue from failing ICM hearts was obtained from individuals undergoing LVAD implantation surgery at the University of Michigan Medical Center. ICM was diagnosed based on known CAD severity that would account for HF. Nonfailing donor hearts (n = 16) were obtained from the University of Wisconsin–Madison Organ and Tissue Donation Program. Donor hearts were stored in cardioplegic solution following removal, then dissected and flash-frozen in liquid nitrogen for storage at –80°C.

Protein extraction. To extract proteins, approximately 15 mg of myocardial tissue from failing ICM and nonfailing donor hearts were cut and pulverized under liquid nitrogen using a CellCrusher kit (Thermo Fisher Scientific; catalog NC1824866). Cryopulverized tissue was resuspended in 1× Dulbecco's Phosphate-Buffered Saline (MilliporeSigma; catalog D1283) supplemented with Halt Protease Inhibitor Cocktail (Thermo Fisher Scientific; catalog 87786) diluted to a final concentration of 1× by vortexing for 10 seconds and then centrifuged at 21,100*g* for 5 minutes. The resulting supernatants (wash) were removed and discarded. To achieve deeper coverage of the cardiac proteome by MS-based proteomics, sequential extraction of proteins was performed with the remaining pellets. Pellets were homogenized in 20 volumes (~300 μL) of LiCl extraction buffer (3 M LiCl, 1 mM TCEP, 10 mM EDTA, and 1× Halt Protease Inhibitor Cocktail from Thermo Fisher Scientific) using a handheld Teflon homogenizer (Bel-Art). Homogenates were vortexed and centrifuged as before, and the resulting supernatants (LiCl extracts) were desalted using Ultra Centrifugal Filter, 10 kDa MWCO filters (MilliporeSigma). The pellets remaining after LiCl extraction were re-homogenized in 20 volumes (~300 μL) of Azo extraction buffer (0.4% Azo from MilliporeSigma, 25 mM ammonium bicarbonate, 1 mM TCEP, 10 mM EDTA, and 1× Halt Protease Inhibitor Cocktail from Thermo Fisher Scientific) using a handheld Teflon homogenizer. Homogenates were subsequently sonicated first via probe sonication (Thermo Fisher Scientific; 20% amplitude, 3 cycles, 3 seconds per cycle) followed by incubation in an ultrasonication bath (Thermo Fisher Scientific) for 30 minutes, followed by incubation in an Eppendorf Thermomixer R at 80°C for 15 minutes. This extract was centrifuged at 21,100*g* for 20 minutes. Then the supernatant was saved and referred to as the Azo extract.

Protein digestion and desalting. All extracts (n = 16 control/LiCl 1; n = 16 control/Azo; n = 16 ICM/LiCl 1; n = 16 ICM/Azo) were normalized to approximately 75 μg of total protein via Bradford protein assay and diluted to the same final concentration (1 mg/mL). LiCl extracts were diluted with 25 mM ammonium bicarbonate and Azo extracts in the remaining 0.4% Azo extraction buffer. For reduction and alkylation of disulfide bonds, samples were treated simultaneously with 25 mM TCEP and 50 mM chloroacetamide and incubated at 37°C and 600 rpm in a Thermomixer R for 30 minutes, after which they were treated with 1 M ammonium bicarbonate to adjust pH to the active range for digestion (~pH 8.5). Digestion was performed by treating samples with a 50:1 (w/w) protein/trypsin ratio and incubating them overnight in a Thermomixer R at 37°C and 600 rpm. Digestion was quenched by addition of formic acid to an approximate final concentration of 0.25% (pH 3–4). Extracts containing Azo were irradiated in front of a UV lamp to degrade surfactant, then centrifuged at 21,100*g* for 30 minutes. All extracts were then desalted by Pierce C18 tips (Thermo Fisher Scientific; catalog 87784) to remove degradation products and other salts, dried, and reconstituted in 0.1% formic acid in water. The peptide content of each sample was assessed using a NanoDrop One/One Microvolume UV-Vis Spectrophotometer (Thermo Fisher Scientific).

Data acquisition. A Bruker timsTOF Pro trapped ion mobility Q-TOF instrument (Billerica) fitted with a captive-spray nano-electrospray ionization source and coupled to a nanoElute nanoflow LC system (Bruker) was used for all analyses. For each sample, a total of 200 ng of peptides was injected onto an Aurora Ultimate C18 column (25 cm length, 75 μm inner diameter, 1.7 μm particle size, 120 Å pore size; IonOpticks). Injections were normalized to achieve a total ion chromatogram intensity of approximately 3×10^7 for each sample. Separations were carried out at a flow rate of 0.4 μL/min and 55°C using a linear gradient increasing from 0% to 17% mobile phase B (0.1% formic acid in acetonitrile) (mobile phase A: 0.1% formic acid in water) over 60 minutes, 17% to 25% from 60 to 90 minutes, 25% to 37% B from 90 to 100 minutes, 37% to 85% B from 100 minutes to 110 minutes, and a 10-minute hold at 85% B before washing and returning to low organic conditions. Mass and tandem mass spectra were obtained in diaPASEF mode, with 32 fragmentation windows 400–1,200 m/z (25 m/z width) and 0.6 to 1.6 $1/K_0$ (0.3 $1/K_0$ width).

Database searching and quantitation. Raw MS data were searched in a library-free manner using DIA-Neural Network (DIANN) (85) version 1.8.1 with the following parameters: 1% FDR, library-free search enabled, Minimum fragment m/z: 200, Maximum fragment m/z: 2,000, N-terminal methionine cleavage enabled, Enzyme: trypsin, Maximum missed cleavages: 1, Minimum peptide length: 7, Maximum peptide length: 40, Minimum precursor m/z: 400, Maximum precursor m/z: 1,400, Minimum precursor charge: 1, Maximum precursor charge: 5, cysteine carbamidomethylation enabled, MS1/MS2 mass accuracy: 10 ppm, Quantification strategy: robust LC (High Precision), Neural network classifier: double-pass mode. All other parameters were left as defaults. Data were searched against a FASTA file containing 20,379 canonical human protein sequences downloaded from UniprotKB. All identified protein groups and corresponding peptides are listed in Supplemental Tables 2 and 3, respectively.

Downstream differential expression analysis was performed as previously described (86). Quantified proteins were filtered for validity using the DAPAR (87) package for R to include all proteins quantified in 8 of 16 runs in at least 1 sample group. After median normalization, imputation of missing values was performed via the ssla algorithm (values partially observed in some replicates of a condition) or set to the quantile below which 2.5% of all observations fall (values that were missing entirely within a condition). Identifications were further filtered to remove any proteins that had imputed values for more than 50% of their quantities in each extract. The DEP R package was used to perform a limma test between all specified contrasts (88, 89), and the IHW (90) R package was used to adjust all P values, using the number of quantified peptides per protein as a covariate. The criteria for significance were 1) an adjusted P value less than 0.05 and 2) a $\log_2$ fold change greater than or equal to 0.6 (approximately equivalent to a 1.5-fold change in the normal scale).

GO and pathway analysis. For GO analysis, proteins differentially expressed in ICM relative to nonfailing donor myocardium were searched in STRING (91), and the functional enrichment categories for biological processes and molecular functions were exported into RStudio. GO terms were filtered to a 1% FDR and plotted using ggplot2 and ggpubr packages (92). Enrichment analysis using active subnetworks was further performed using the package pathfindR (34) using the KEGG as the gene set and a P value threshold of 5%. Results were plotted similarly to the GO analyses. Protein-protein interaction networks from STRING were visualized using Cytoscape (93). ECM proteins and categorical information were retrieved from MatrisomeDB (25).

Statistics. This study used limma in all assessments of protein differential expression, and *P* values were adjusted using independent hypothesis weighting with peptide number as the covariate. Unless otherwise stated, the *P* value threshold for significance was 0.05, and the log fold change threshold was 0.6. Pathway analyses using pathfindR used the default package settings to test pathway enrichment and the default *P* value adjustment of Bonferroni. Error bars in the inset bar plot of Figure 1C represent mean + standard error of the mean. Error bars in Figure 3A represent the mean ± the 97.5% confidence interval (critical *t* score at 97.5% confidence multiplied by standard error of the mean).

Study approval. The procedures for the collection of human failing ICM and nonfailing donor heart tissues were approved by the Institutional Review Boards (IRBs) of the University of Wisconsin–Madison and the University of Michigan, Ann Arbor, Michigan, USA, respectively. Written informed consent was obtained from participants for all the ICM samples. For nonfailing control samples obtained from deceased donor hearts, the requirement for informed consent was waived by the IRB.

Data availability. The MS proteomics data have been deposited to the ProteomeXchange Consortium with the data set identifier PXD064211 and MassIVE repository with identifier MSV000097977. Patient information (Supplemental Table 1), peptide precursors from DIANN (Supplemental Table 2), protein groups identified from database search (Supplemental Table 3), and DAVID GO enrichment results (Supplemental Table 4) are available as supplemental information. Any other data, such as scripts used in data analysis, are available upon request from the authors.

Author contributions

All listed authors have made substantial contributions to the study. KMB led experimental design, data acquisition and analysis, and manuscript writing. HTR, AJP, ZRG, MWM, TJA, ZG, EAC, and SJP contributed to data generation, data interpretation, and manuscript editing. IL and PCT helped design the study and provided essential patient samples. YG conceived the study, supervised all aspects of the project, provided intellectual guidance, and edited and finalized the manuscript.

Funding support

This work is the result of NIH funding, in whole or in part, and is subject to the NIH Public Access Policy. Through acceptance of this federal funding, the NIH has been given a right to make the work publicly available in PubMed Central.

- NIH R01HL109810 (to YG).
- YG by NIH R01GM117058 and S10OD018475.
- EAC by NIH Chemistry-Biology Interface Training Program NIH T32GM008505.
- TJA by Training Program in Molecular and Cellular Pharmacology, NIH T32GM008688-20.
- HTR by the National Heart, Lung, and Blood Institute of the NIH under T32HL007936 through the University of Wisconsin–Madison Cardiovascular Research Center.
- PCT by NIH R01HL164416 and R01HL166140

Acknowledgments

We would like to express sincere gratitude to the donor and their loved ones for the generous tissue donation. We thank James Anderson and Erin Halpin at the University of Wisconsin Organ and Tissue Donation for coordination of donor heart collection.

Address correspondence to: Ying Ge, 1111 Highland Ave., WIMR II 8551, Madison, Wisconsin 53705, USA. Email: ying.ge@wisc.edu.

1. Nowbar AN, et al. Mortality from ischemic heart disease. *Circ Cardiovasc Qual Outcomes*. 2019;12(6):e005375.
2. Savarese G, et al. Global burden of heart failure: a comprehensive and updated review of epidemiology. *Cardiovasc Res*. 2023;118(17):3272–3287.
3. Pastena P, et al. Ischemic cardiomyopathy: epidemiology, pathophysiology, outcomes, and therapeutic options. *Heart Fail Rev*. 2024;29(1):287–299.
4. Briceno N, et al. Ischaemic cardiomyopathy: pathophysiology, assessment and the role of revascularisation. *Heart*. 2016;102(5):397–406.
5. Felker GM, et al. A standardized definition of ischemic cardiomyopathy for use in clinical research. *J Am Coll Cardiol*. 2002;39(2):210–218.

6. Mouw JK, et al. Extracellular matrix assembly: a multiscale deconstruction. *Nat Rev Mol Cell Biol*. 2014;15(12):771–785.
7. Naba A. Mechanisms of assembly and remodelling of the extracellular matrix. *Nat Rev Mol Cell Biol*. 2024;25(11):865–885.
8. Nagaraju CK, et al. Myofibroblast phenotype and reversibility of fibrosis in patients with end-stage heart failure. *J Am Coll Cardiol*. 2019;73(18):2267–2282.
9. Ma Y, et al. Cardiac fibroblast activation post-myocardial infarction: current knowledge gaps. *Trends Pharmacol Sci*. 2017;38(5):448–458.
10. Weber KT, et al. Myofibroblast-mediated mechanisms of pathological remodelling of the heart. *Nat Rev Cardiol*. 2013;10(1):15–26.
11. Frangogiannis NG. Matricellular proteins in cardiac adaptation and disease. *Physiol Rev*. 2012;92(2):635–688.
12. Frangogiannis NG. The extracellular matrix in ischemic and nonischemic heart failure. *Circ Res*. 2019;125(1):117–146.
13. Naba A. Ten years of extracellular matrix proteomics: accomplishments, challenges, and future perspectives. *Mol Cell Proteomics*. 2023;22(4):100528.
14. McCabe MC, et al. Mass spectrometry-based atlas of extracellular matrix proteins across 25 mouse organs. *J Proteome Res*. 2023;22(3):790–801.
15. Knott SJ, et al. Photocleavable surfactant-enabled extracellular matrix proteomics. *Anal Chem*. 2020;92(24):15693–15698.
16. Barallobre-Barreiro J, et al. Proteomics analysis of cardiac extracellular matrix remodeling in a porcine model of ischemia/reperfusion injury. *Circulation*. 2012;125(6):789–802.
17. Lindsey ML, et al. Proteomic analysis of the cardiac extracellular matrix: clinical research applications. *Expert Rev Proteomics*. 2018;15(2):105–112.
18. Barallobre-Barreiro J, et al. Extracellular matrix in heart failure: role of ADAMTS5 in proteoglycan remodeling. *Circulation*. 2021;144(25):2021–2034.
19. De Castro Brás LE, et al. Texas 3-step decellularization protocol: looking at the cardiac extracellular matrix. *J Proteomics*. 2013;86:43–52.
20. Barallobre-Barreiro J, et al. A sequential extraction methodology for cardiac extracellular matrix prior to proteomics analysis. *Methods Mol Biol*. 2013;1005:215–223.
21. Brown KA, et al. A photocleavable surfactant for top-down proteomics. *Nat Methods*. 2019;16(5):417–420.
22. Bayne EF, et al. High-throughput extracellular matrix proteomics of human lungs enabled by photocleavable surfactant and diaPASEF. *J Proteome Res*. 2024;23(8):2908–2918.
23. Kelleher SD, Hultin HO. Lithium chloride as a preferred extractant of fish muscle proteins. *J Food Sci*. 1991;56(2):315–317.
24. Chapman EA, et al. Structure and dynamics of endogenous cardiac troponin complex in human heart tissue captured by native nanoproteomics. *Nat Commun*. 2023;14(1):8400.
25. Shao X, et al. MatrisomeDB: the ECM-protein knowledge database. *Nucleic Acids Res*. 2020;48(d1):D1136–D1144.
26. Lopaschuk GD, et al. Cardiac energy metabolism in heart failure. *Circ Res*. 2021;128(10):1487–1513.
27. Greene AG, et al. Lysyl oxidase like 1: biological roles and regulation. *Exp Eye Res*. 2020;193:107975.
28. Cangemi C, et al. Fibulins and their role in cardiovascular biology and disease. *Adv Clin Chem*. 2014;67:245–265.
29. Happonen KE, et al. Interactions of the complement system with molecules of extracellular matrix: relevance for joint diseases. *Immunobiology*. 2012;217(11):1088–1096.6.
30. Park S, et al. Cardiac fibrosis is associated with decreased circulating levels of full-length CILP in heart failure. *JACC Basic Transl Sci*. 2020;5(5):432–443.
31. Frangogiannis N. Transforming growth factor-β in tissue fibrosis. *J Exp Med*. 2020;217(3):e20190103.
32. Bujak M, Frangogiannis NG. The role of TGF-beta signaling in myocardial infarction and cardiac remodeling. *Cardiovasc Res*. 2007;74(2):184–195.
33. Huang DW, et al. Systematic and integrative analysis of large gene lists using DAVID bioinformatics resources. *Nat Protoc*. 2009;4(1):44–57.
34. Ulgen E, et al. pathfindR: an R package for comprehensive identification of enriched pathways in omics data through active subnetworks. *Front Genet*. 2019;10:858.
35. Eden M, et al. Cardiac Mechanoperception and Mechanotransduction: Mechanisms of Stretch Sensing in Cardiomyocytes and Implications for Cardiomyopathy. In: Hecker M, Duncker DJ, eds. *Cardiac Mechanobiology in Physiology and Disease*. Springer International Publishing; 2023:1–35.
36. Beltrami CA, et al. Structural basis of end-stage failure in ischemic cardiomyopathy in humans. *Circulation*. 1994;89(1):151–163.
37. Fomovsky GM, et al. Contribution of extracellular matrix to the mechanical properties of the heart. *J Mol Cell Cardiol*. 2010;48(3):490–496.
38. Sewanan LR, et al. Extracellular matrix from hypertrophic myocardium provokes impaired twitch dynamics in healthy cardiomyocytes. *JACC Basic Transl Sci*. 2019;4(4):495–505.
39. Sharp WW, et al. Mechanical forces regulate focal adhesion and costamere assembly in cardiac myocytes. *Am J Physiol*. 1997;273(2 pt 2):H546–H556.
40. Dowling JJ, et al. Kindlin-2 is an essential component of intercalated discs and is required for vertebrate cardiac structure and function. *Circ Res*. 2008;102(4):423–431.
41. Zhang Z, et al. Postnatal loss of Kindlin-2 leads to progressive heart failure. *Circ Heart Fail*. 2016;9(8):e003129.
42. Moser M, et al. Kindlin-3 is essential for integrin activation and platelet aggregation. *Nat Med*. 2008;14(3):325–330.
43. Wen L, et al. Kindlin-3 recruitment to the plasma membrane precedes high-affinity β2-integrin and neutrophil arrest from rolling. *Blood*. 2021;137(1):29–38.
44. Oksala N, et al. Kindlin 3 (FERMT3) is associated with unstable atherosclerotic plaques, anti-inflammatory type II macrophages and upregulation of beta-2 integrins in all major arterial beds. *Atherosclerosis*. 2015;242(1):145–154.
45. Penna C, et al. Overexpression of the muscle-specific protein, melusin, protects from cardiac ischemia/reperfusion injury. *Basic Res Cardiol*. 2014;109(4):418.
46. Frangogiannis NG. The inflammatory response in myocardial injury, repair, and remodelling. *Nat Rev Cardiol*. 2014;11(5):255–265.
47. Brown KA, et al. High-throughput proteomics enabled by a photocleavable surfactant. *Angew Chem Int Ed Engl*. 2020;59(22):8406–8410.

48. Shahinian JH, et al. Proteomics highlights decrease of matricellular proteins in left ventricular assist device therapy†. *Eur J Cardiothorac Surg*. 2017;51(6):1063–1071.
49. De Weger RA, et al. Proteomic profiling of the human failing heart after left ventricular assist device support. *J Heart Lung Transplant*. 2011;30(5):497–506.
50. Rienks M, et al. Myocardial extracellular matrix: an ever-changing and diverse entity. *Circ Res*. 2014;114(5):872–888.
51. Christensen G, et al. Sweet, yet underappreciated: proteoglycans and extracellular matrix remodeling in heart disease. *Matrix Biol*. 2019;75–76:286–299.
52. Li L, et al. Extracellular matrix remodeling and cardiac fibrosis. *Matrix Biol*. 2018;68–69:490–506.
53. González A, et al. The complex dynamics of myocardial interstitial fibrosis in heart failure. Focus on collagen cross-linking. *Biochim Biophys Acta Mol Cell Res*. 2019;1866(9):1421–1432.
54. López B, et al. Myocardial collagen cross-linking is associated with heart failure hospitalization in patients with hypertensive heart failure. *J Am Coll Cardiol*. 2016;67(3):251–260.
55. Frangogiannis NG. The extracellular matrix in myocardial injury, repair, and remodeling. *J Clin Invest*. 2017;127(5):1600–1612.
56. Wohlgemuth RP, et al. Alignment, cross linking, and beyond: a collagen architect's guide to the skeletal muscle extracellular matrix. *Am J Physiol Cell Physiol*. 2023;325(4):C1017–C1030.
57. Mukherjee D, Sen S. Alteration of collagen phenotypes in ischemic cardiomyopathy. *J Clin Invest*. 1991;88(4):1141–1146.
58. Weber KT, et al. Patterns of myocardial fibrosis. *J Mol Cell Cardiol*. 1989;21 Suppl 5:121–131.
59. Bray M-A, et al. Sarcomere alignment is regulated by myocyte shape. *Cell Motil Cytoskeleton*. 2008;65(8):641–651.
60. Hinz B, et al. Recent developments in myofibroblast biology: paradigms for connective tissue remodeling. *Am J Pathol*. 2012;180(4):1340–1355.
61. Goldsmith EC, et al. Myocardial fibroblast-matrix interactions and potential therapeutic targets. *J Mol Cell Cardiol*. 2014;70:92–99.
62. Naugle JE, et al. Type VI collagen induces cardiac myofibroblast differentiation: implications for postinfarction remodeling. *Am J Physiol Heart Circ Physiol*. 2006;290(1):H323–H330.
63. Luther DJ, et al. Absence of type VI collagen paradoxically improves cardiac function, structure, and remodeling after myocardial infarction. *Circ Res*. 2012;110(6):851–856.
64. Chen S, Birk DE. The regulatory roles of small leucine-rich proteoglycans in extracellular matrix assembly. *FEBS J*. 2013;280(10):2120–2137.
65. Huang C, et al. Asporin, an extracellular matrix protein, is a beneficial regulator of cardiac remodeling. *Matrix Biol*. 2022;110:40–59.
66. Ferdous Z, et al. Decorin-transforming growth factor- interaction regulates matrix organization and mechanical characteristics of three-dimensional collagen matrices. *J Biol Chem*. 2007;282(49):35887–35898.
67. Annes JP, et al. Integrin alphaVbeta6-mediated activation of latent TGF-beta requires the latent TGF-beta binding protein-1. *J Cell Biol*. 2004;165(5):723–734.
68. Humeres C, et al. Smad-dependent pathways in the infarcted and failing heart. *Curr Opin Pharmacol*. 2022;64:102207.
69. Hinz B. The extracellular matrix and transforming growth factor-β1: tale of a strained relationship. *Matrix Biol*. 2015;47:54–65.
70. Maeda T, et al. Conversion of mechanical force into TGF-β-mediated biochemical signals. *Curr Biol*. 2011;21(11):933–941.
71. Border WA, Noble NA. Interactions of transforming growth factor-beta and angiotensin II in renal fibrosis. *Hypertension*. 1998;31(1 pt 2):181–188.
72. Sweetwyne MT, Murphy-Ullrich JE. Thrombospondin1 in tissue repair and fibrosis: TGF-β-dependent and independent mechanisms. *Matrix Biol*. 2012;31(3):178–186.
73. Chistiakov DA, et al. Thrombospondins: a role in cardiovascular disease. *Int J Mol Sci*. 2017;18(7):1540.
74. Schips TG, et al. Thrombospondin-3 augments injury-induced cardiomyopathy by intracellular integrin inhibition and sarcolemmal instability. *Nat Commun*. 2019;10(1):76.
75. Chen Y, et al. Correlation between low THBS3 expression in peripheral blood and acute myocardial infarction. *Front Biosci (Landmark Ed)*. 2022;27(10):291.
76. Cabac-Pogorevici I, et al. Ischaemic cardiomyopathy. Pathophysiological insights, diagnostic management and the roles of revascularisation and device treatment. Gaps and dilemmas in the era of advanced technology. *Eur J Heart Fail*. 2020;22(5):789–799.
77. Frangogiannis NG, et al. Active interstitial remodeling: an important process in the hibernating human myocardium. *J Am Coll Cardiol*. 2002;39(9):1468–1474.
78. Masaki M, et al. Smad1 protects cardiomyocytes from ischemia-reperfusion injury. *Circulation*. 2005;111(21):2752–2759.
79. Jenkins G. The role of proteases in transforming growth factor-beta activation. *Int J Biochem Cell Biol*. 2008;40(6–7):1068–1078.
80. Klingberg F, et al. Prestress in the extracellular matrix sensitizes latent TGF-β1 for activation. *J Cell Biol*. 2014;207(2):283–297.
81. Regitz-Zagrosek V. Sex and gender differences in heart failure. *Int J Heart Fail*. 2020;2(3):157–181.
82. EUGenMed Cardiovascular Clinical Study Group, et al. Gender in cardiovascular diseases: impact on clinical manifestations, management, and outcomes. *Eur Heart J*. 2016;37(1):24–34.
83. Towler AG, et al. A single-step protein extraction for lung extracellular matrix proteomics enabled by the photocleavable surfactant Azo and timsTOF pro. *Mol Cell Proteomics*. 2025;24(8):100950.
84. Neff LS, Bradshaw AD. Cross your heart? Collagen cross-links in cardiac health and disease. *Cell Signal*. 2021;79:109889.
85. Demichev V, et al. DIA-NN: neural networks and interference correction enable deep proteome coverage in high throughput. *Nat Methods*. 2020;17(1):41–44.
86. Mann MW, et al. Bromodomain-containing Protein 4 regulates innate inflammation via modulation of alternative splicing. *Front Immunol*. 2023;14:1212770.
87. Wieczorek S, et al. DAPAR & ProStaR: software to perform statistical analyses in quantitative discovery proteomics. *Bioinformatics*. 2017;33(1):135–136.
88. Feng Z, et al. DEP2: an upgraded comprehensive analysis toolkit for quantitative proteomics data. *Bioinformatics*. 2023;39(8):btad526.
89. Ritchie ME, et al. limma powers differential expression analyses for RNA-sequencing and microarray studies. *Nucleic Acids Res*. 2015;43(7):e47.

90. Ignatiadis N, et al. Data-driven hypothesis weighting increases detection power in genome-scale multiple testing. *Nat Methods*. 2016;13(7):577–580.
91. Szklarczyk D, et al. The STRING database in 2023: protein-protein association networks and functional enrichment analyses for any sequenced genome of interest. *Nucleic Acids Res*. 2023;51(d1):D638–D646.
92. Kassambara A. ggpubr: "ggplot2" Based Publication Ready Plots. https://cran.r-project.org/web/packages/ggpubr/index.html. Published June 27, 2025. Accessed September 29, 2025.
93. Shannon P, et al. Cytoscape: a software environment for integrated models of biomolecular interaction networks. *Genome Res*. 2003;13(11):2498–2504.